

The 2005 Qeshm Island earthquake (Iran)—a link between buried reverse faulting and surface folding in the Zagros Simply Folded Belt?

Edwin Nissen,¹ Manoucher Ghorashi,² James Jackson,³ Barry Parsons¹ and Morteza Talebian²

¹COMET, Department of Earth Sciences, Parks Road, Oxford OX1 3PR, UK. E-mail: ed.nissen@earth.ox.ac.uk

²Geological Survey of Iran, PO Box 13185-1494, Tehran, Iran

³COMET, Bullard Laboratories, Madingley Road, Cambridge CB3 0EZ, UK

Accepted 2007 May 30. Received 2007 May 30; in original form 2007 February 20

SUMMARY

The 2005 November 27 Qeshm Island earthquake (M_w 6.0) provides an excellent opportunity to study coseismic deformation in the Zagros Simply Folded Belt with Synthetic Aperture Radar interferometry (InSAR). Typical of reverse faulting in the Zagros, slip in the Qeshm Island earthquake did not rupture the surface. However, ascending and descending track interferograms spanning the earthquake both show an elliptical pattern of surface deformation in the central part of the island. We invert the interferometric data to attain a set of source parameters; these show ~ 1 m slip on a steep ($\sim 50^\circ$), north-dipping reverse fault, extending from a maximum depth of ~ 8 up to ~ 4 km below the surface. Limited aeromagnetic data suggests the fault ruptured the sedimentary cover; whether its deepest parts also affected the crystalline basement is not clear. Source parameters from seismic body wave modelling agree with those from the interferometric modelling. Using the InSAR-derived model, we produce a map of coseismic vertical displacements, with which we compare the surface structure of the island. Coseismic uplift is centred on the eastern end of a major anticline, which trends E–W, parallel with the fault. The long-term growth of this fold may be controlled primarily by repeated earthquakes on this fault. However, the uplifted region extends to parts of other nearby folds, whose long-term growth must have other controls; moreover, a region of coseismic subsidence lies very close to a part of the Qeshm island coastline that displays raised beaches, evidence of Quaternary uplift. Therefore the link between reverse faulting and surface folding is not wholly evident from this earthquake alone. The local structure is complicated by orthogonal fold axes; it may take a large earthquake in a simpler structural setting within the Zagros to establish convincingly whether a one-to-one correlation between faulting and folding exists.

Key words: active tectonics, earthquake source parameters, faulting, folding, InSAR, Zagros.

1 INTRODUCTION

The Zagros mountains in southern Iran are one of the most seismically active regions in the Alpine–Himalayan belt, accommodating approximately one-third of the N–S shortening between the Arabian Plate and Eurasia, which is ~ 25 mm yr⁻¹ at 56° E (Sella *et al.* 2002; Vernant *et al.* 2004). Though strike-slip earthquakes have an important role in the central and western parts of the range, where convergence is oblique, seismicity in the Zagros is dominated by high-angle reverse faulting (Talebian & Jackson 2004). These earthquakes only rarely rupture the surface (Walker *et al.* 2005); near-surface deformation is instead taken up by folding, which has produced the spectacular whaleback anticlines and synclines (often > 100 km in length) that dominate the topography of the Simply Folded Belt, the southwestern part of the Zagros (Fig. 1). There has

long been a question as to whether there is a one-to-one correlation between these anticlines and steep, seismogenic reverse faults beneath them (e.g. Falcon 1969; Jackson 1980).

In some regions of continental shortening, a causal relationship between buried thrust faulting and surface folding is known to exist; coseismic fold growth above a blind thrust fault was first observed during the M_s 7.3 1980 El Asnam earthquake in Algeria (Yielding *et al.* 1981) and has since been demonstrated in eastern Iran (Berberian *et al.* 2000; Walker *et al.* 2003; Parsons *et al.* 2006), amongst other places. In the Zagros, however, it has been difficult to establish whether such a relationship exists. This is largely because of uncertainty in the extent to which the sedimentary cover is decoupled from its underlying basement by various décollement horizons, particularly in evaporites, that extend across large parts of the range.

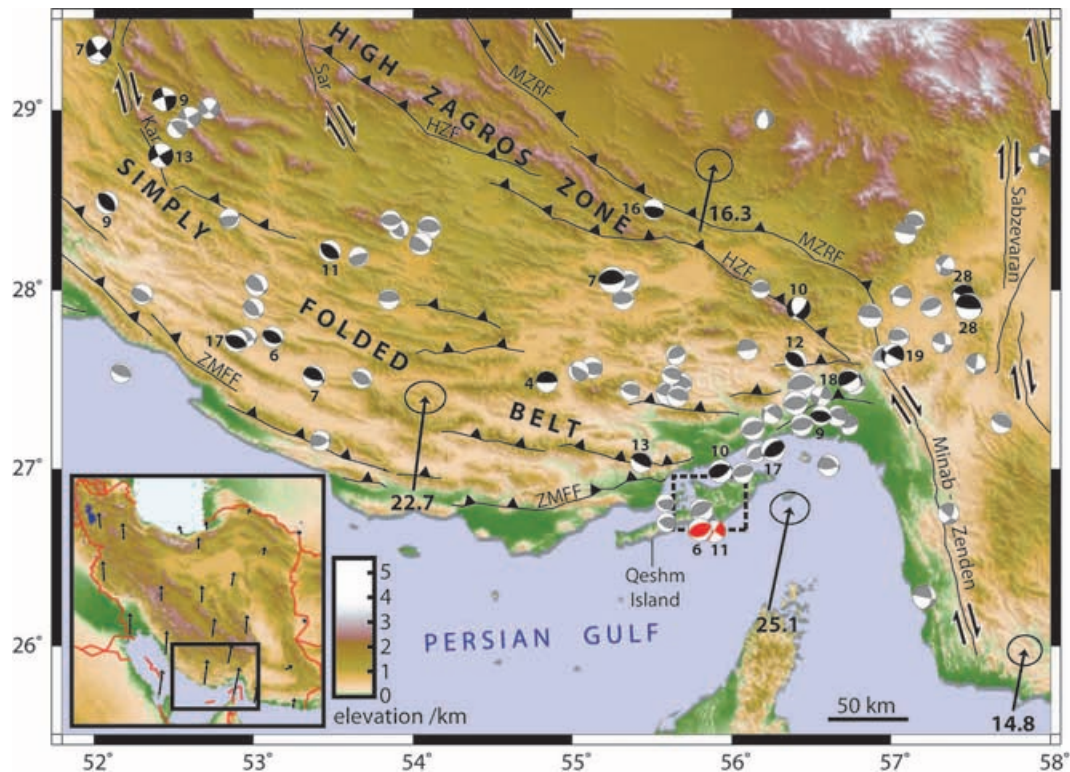


Figure 1. Shaded relief topography of the SE Zagros mountains in a Mercator projection. The inset shows the location of the map within Iran, with arrows representing GPS velocities relative to stable Eurasia (Vernant *et al.* 2004). In the main map, these same GPS velocities (mm yr^{-1}) are shown with 95 per cent confidence ellipses. Grey focal mechanisms are Harvard CMT solutions (1976–2006). Black ones are body wave solutions for earthquakes in the same period (as listed in Talebian & Jackson 2004), with their centroid depths (in km) next to them. The two red focal mechanisms are our preferred body wave solutions for the 2005 November 27 M_w 6.0 Qeshm earthquake (centroid depth fixed to 6 km; see Section 3.3) and the M_w 5.4 aftershock. Black lines show major active faults; MZRF = Main Zagros Reverse Fault, HZF = High Zagros Fault, Kar = Karebas Fault, Sar = Sarvestan Fault, ZMFF = Zagros Mountain Front Fault. The dashed box over Qeshm island shows the extents of Figs 2, 5, 7 and 11.

Synthetic Aperture Radar interferometry (InSAR) can potentially help resolve this question. Coseismic surface displacements, imaged to subcentimetric precision with InSAR, can be compared with the location of surface folding; a strong link between the two would suggest that fold growth is controlled by faulting during earthquakes. However, since earthquakes were first studied using this method 15 yr ago, there have been very few events in the Zagros of sufficient magnitude for detailed interferometric analysis. Lohman & Simons (2005) use InSAR to locate four $M_w \sim 5$ earthquakes in the Zagros, but in each case interferograms in only one satellite line-of-sight (LOS) direction are produced, providing little constraint on the mechanisms of such small events. The M_w 6.0 2005 November 27 Qeshm Island earthquake, however, provides one of the first opportunities to study the surface deformation of a large earthquake in the Zagros with InSAR. In this paper, we combine radar interferometry with seismology and field observations to estimate the source characteristics of this earthquake and investigate the resulting surface displacements.

2 OVERVIEW OF QESHM ISLAND

Qeshm Island lies in the eastern Persian Gulf, ~ 10 km off the Iranian mainland (Fig. 1). It is ~ 110 km in length but as little as ~ 10 km wide, and trends $\sim \text{ENE}$, parallel with the mainland coast. The surface geology mainly comprises Neogene marls and sandstones, folded into prominent anticlines and synclines. Evaporites

outcrop in the far western part of the island, where a prominent salt dome (Kuh-e-Namakdan) brings Cambrian Hormuz salt to the surface as a diapir. This is one of many similar salt domes in the Simply Folded Belt. On the adjacent mainland, Hormuz salt also outcrops in the cores of many whaleback anticlines. It is possible that the Qeshm island anticlines may also be cored with evaporites, although (Kuh-e-Namakdan aside) no salt is currently exposed at the surface. The depth to the basement on the island is not known specifically, but aeromagnetic surveys of the mainland Zagros (Kugler 1973; Morris 1977) may offer a rough indication. Spectral analysis of these data reveals a basement depth of ~ 16 km on the mainland just NW of Qeshm Island, while application of the half-slope method to individual magnetic anomalies yields depths of 10–17 km in the same area (Talebian 2003). However, these estimates rely on long wavelength magnetic signals and locally there may be departures from this range.

Overall, Qeshm Island bears many geological and structural similarities with the adjacent mainland, and can thus be considered part of the Zagros Simply Folded Belt. Unusually, however, fold axes on Qeshm Island do not follow parallel trends. Instead, folds trending $\sim \text{E-W}$ (Salakh anticline), $\sim \text{NE-SW}$ (Ramkan syncline and Suza anticline) and $\sim \text{NW-SE}$ (Laft anticline) converge to form a complicated structure in the central part of the island (Fig. 2).

Extensive marine terraces indicate that much of Qeshm island has been undergoing uplift during Quaternary times (Haghipour & Fontugne 1993). The terraces comprise reef and beach deposits lying uncomfortably over Neogene sediments. As many as 18 separate

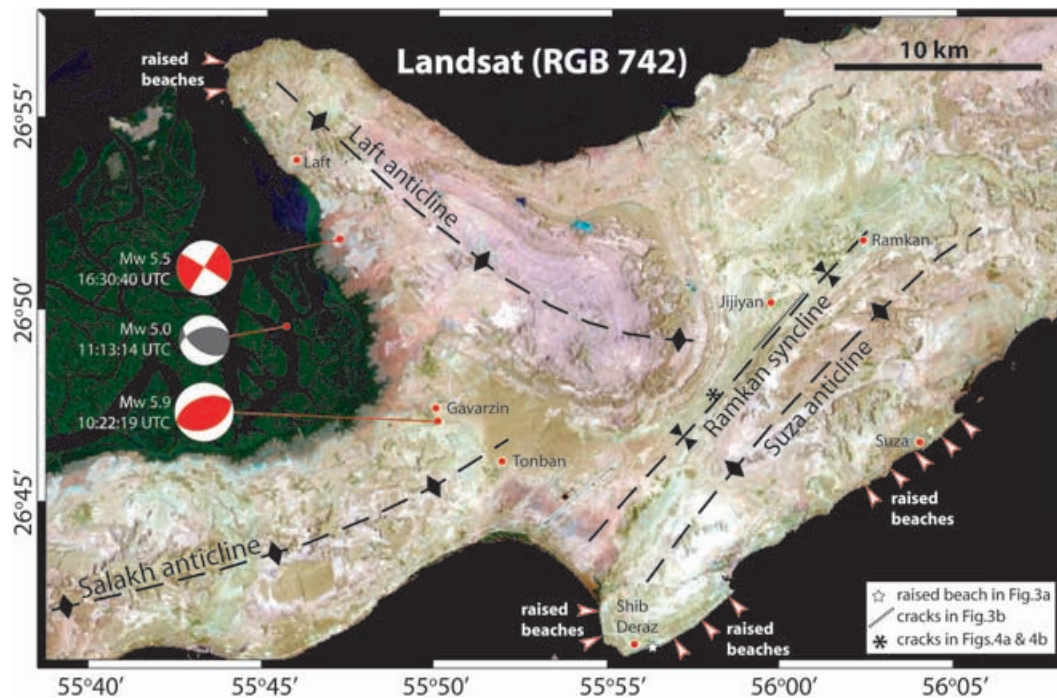


Figure 2. Landsat image (RGB 742) of central Qeshm island, displayed in the local UTM zone (40) projection (as are subsequent maps). The red focal mechanisms are our preferred body wave solutions for the 2005 November 27 M_w 6.0 Qeshm Island earthquake and the M_w 5.4 aftershock, while the grey mechanism is the Harvard CMT solution for the M_w 5.0 aftershock. Red lines connect these earthquakes to their hypocenters, as listed in the updated version of the Engdahl *et al.* (1998) catalogue; these are likely to be accurate to around ~ 10 – 15 km, from InSAR studies of other earthquakes in Iran (Talebian *et al.* 2004, 2006; Lohman & Simons 2005; Parsons *et al.* 2006). Major fold axes are marked with dashed black lines. Red arrows point to parts of the Qeshm coastline that show evidence of active uplift (from Haghipour & Fontugne 1993); the star indicates the location of the photograph in Fig. 3(a). The short dotted line represents the cracks in Fig. 3(b), and the asterisk shows the location of the cracks in Figs 4(a) and (b).

levels have been mapped, the oldest at 220 m altitude and the youngest in the current littoral zone. Uranium-series dating of aragonitic corals yields uplift rates of 0.2 mm yr^{-1} (Preusser *et al.* 2003). In the central part of the island, raised beaches along the coastlines near Shib Deraz, Suza and north of Laft, indicate continuing uplift at the present-day (Figs 2 and 3a).

3 THE QESHM ISLAND EARTHQUAKE

On 2005 November 27 at 10:22:19 UTC (13:52:19 local time), a M_w 6.0 earthquake struck Qeshm island. It destroyed the village of Tonban in the central part of the island, while several neighbouring settlements including Gavarzin and Jijyan were badly damaged. Overall, 13 people were killed and a further ~ 100 injured; these figures would probably have been higher had the earthquake not struck in the middle of the day, when many people were outdoors. Several aftershocks followed, including events of M_w 5.0 and 5.4 on the same day at 11:13:14 and 16:30:40 UTC, respectively.

In this section, we begin by discussing field observations of ground deformation following the earthquake. We then produce ascending and descending-track interferograms spanning the earthquake; modelling these displacements using elastic dislocation theory, we attain a set of source parameters. We then model the earthquake and its largest aftershock with P and SH body waves to provide a second, independent set of source parameters.

3.1 Field observations

Two of us (MG and MT) visited Qeshm Island immediately after the earthquake; three of us (MG, JJ and MT) returned in 2006 May. No

coseismic surface ruptures were observed, nor were any reported by local people. However, we did spot two interesting surface deformational features that may or may not have resulted from the Qeshm earthquake.

First, parallel sets of cracks were seen in the northwestern limb of the Ramkan syncline, close to the fold axis (Figs 2 and 3b). Local people said these appeared after the earthquake. They are minor shortening features representing buckling or fracture of the top 2–3 cm of salt-encrusted soil. They can be followed for ~ 3 km along a 040° trend, parallel with the strike of the bedding in the syncline but oblique to the E–W fault planes of our InSAR and body wave models of the earthquake (see Sections 3.2 and 3.3). This suggests that the cracks are not a direct continuation of the faulting at depth. Instead, they are likely to represent flexural slip along bedding planes, possibly indicating the tightening of the Ramkan syncline during the earthquake. A similar style of surface deformation has been reported for some other reverse faulting earthquakes in Iran, such as the 1978 September 16 M_s 7.4 Tabas earthquake (Berberian 1979; Walker *et al.* 2003).

Secondly, a small set of cracks were seen further southwest within the Ramkan syncline (Figs 2, 4a and b). They are tensional fissures, only 100–200 m in length and trending 120° , oblique to both the local structure and to the fault planes of our earthquake models. Two of the cracks were observed during an earlier field trip in 2005 January (MT), several months before the earthquake (Fig. 4a). We revisited the same locality shortly after the earthquake and noted a third crack had appeared, 1 m southwest of the earlier cracks (Fig. 4b). However, this latest opening was not necessarily a result of the earthquake. Similar cracks appear and disappear frequently on Qeshm island, whether or not there have been earthquakes. Indeed,



Figure 3. (a) View NE from 26°41'22'' N 55°56'18'' E (the star in Fig. 2), showing raised beaches, tilted gently seawards (to the SE), on the coastline east of Shib Deraz. (b) View SW from 26°50'07'' N 56°00'35''E. These parallel sets of cracks, trending 040°, appeared after the Qeshm Island earthquake in the northwestern limb of the Ramkan syncline (see dashed line in Fig. 2). The hills on the left of the picture are NW-dipping beds in the opposite limb of the same syncline.

we observed several others in many different parts of the island in 2005 January; one such example is shown in Fig. 4(c). These cracks often follow pre-existing jointing, and may be related to subsurface salt movement.

3.2 SAR interferometry

We use the JPL/Caltech ROI-PAC software (Rosen *et al.* 2004) and the Envisat ASAR data itemized in the top part of Table 1 to pro-

duce three interferograms spanning the earthquake. Two of these are descending track interferograms with a centre-scene incidence angle of 23° (beam mode IS2), while the third is an ascending track interferogram with an incidence angle of 41° (beam mode IS6). Two out of three interferograms span 350 d, while one descending-track interferogram spans just 35 d. We use precise orbits provided by ESA, but make no further orbital adjustments. The topographic phase contribution is removed using the 3-arcsec (90 m) resolution Shuttle Radar Topographic Mission (SRTM) DEM (Farr & Kobrick

Table 1. Summary of Envisat data used to produce interferograms. *Mode* is the Envisat acquisition mode and *i* is the incidence angle at the centre of the image, measured from the vertical. The first image of each pair was acquired on Date 1, and the second on Date 2, separated by Δt (d). The perpendicular baseline between the orbits in each pass is B_{\perp} (m), and the altitude of ambiguity H_a (m). The top three interferograms span the earthquake; the bottom two cover periods before and after the earthquake, respectively.

Pass	Mode	<i>i</i>	Track	Date 1	Orbit 1	Date 2	Orbit 2	Δt (d)	B_{\perp} (m)	H_a (m)
Desc.	IS2	23	435	24-Nov-05	19 527	29-Dec-05	20 028	35	197	48
Desc.	IS2	23	435	17-Feb-05	15 519	02-Feb-06	20 529	350	65	145
Asc.	IS6	41	328	05-Jan-05	14 911	21-Dec-05	19 921	350	37	254
Desc.	IS2	23	435	17-Jun-04	12 012	24-Nov-05	19 527	525	26	362
Desc.	IS2	23	435	29-Dec-05	20 028	09-Mar-06	21 030	70	67	140

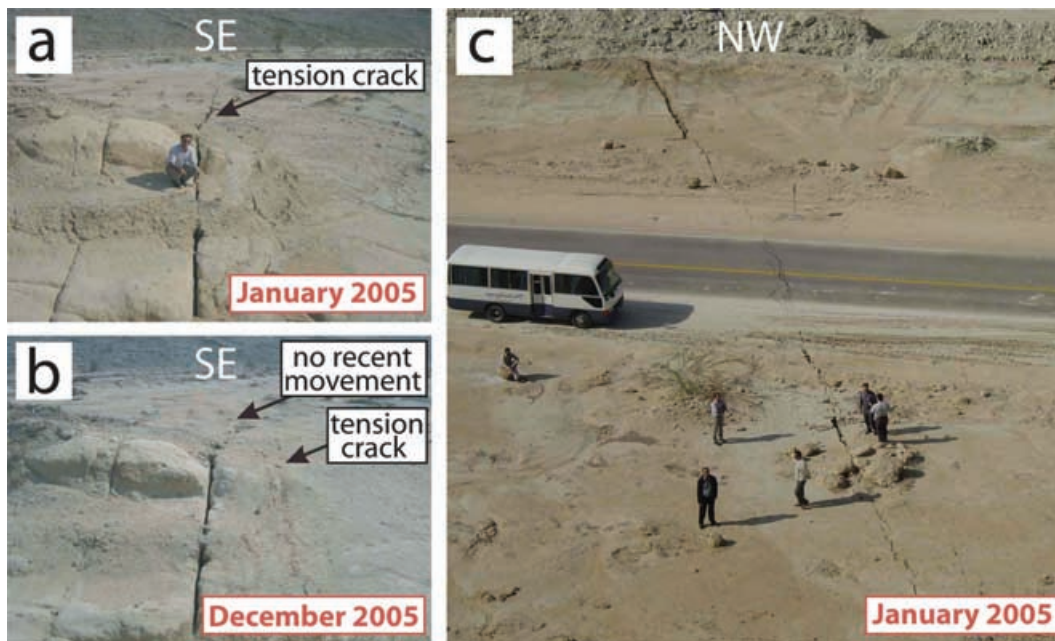


Figure 4. (a) Photo taken in January 2005, facing SE from $26^{\circ}47'47''$ N $55^{\circ}58'07''$ E (the asterisk in Fig. 2) of cracks trending 120° . (b) The same view in 2005 December, shortly after the Qeshm Island earthquake. A new crack has appeared, 1 m to the SW of the earlier ones. This opening may or may not be a result of the earthquake; similar cracks appear and disappear frequently on Qeshm island. An example of these is shown in (c): photo taken in 2005 January, facing NW from $26^{\circ}48'22''$ N $55^{\circ}58'04''$ E, ~ 1 km north of (a). This tension fissure appeared approximately 1 yr before the Qeshm Island earthquake; it trends 110° and has opened by ~ 5 cm.

2000), and a power spectrum filter is used to smooth the interferograms (Goldstein & Werner 1998).

The 350-d ascending-track interferogram is shown in Fig. 5(a) and the 350-d descending track interferogram in Fig. 5(b). The 35-d descending-track interferogram looks very similar in shape to the 350-d one; for comparison it is shown later on (in Fig. 7a). They are displayed wrapped, adjacent fringes differing by 2.8 cm in LOS displacement. They each have excellent correlation over Qeshm island, which is low-lying and sparsely vegetated.

All three interferograms display a roughly elliptical pattern of fringes, elongated in an E–W orientation and containing displacements towards the satellite. In the ascending-track interferogram, maximum displacements are ~ 14 cm (5 fringes) at $26^{\circ}49'N$ $55^{\circ}54'E$. In the descending case, peak displacements are greater— ~ 17 cm (6 fringes) in the 35-d interferogram and ~ 20 cm (7 fringes) in the 350-d interferogram—and centred further east, at $26^{\circ}49'N$ $55^{\circ}56'E$.

All three interferograms also display an area of displacements away from the satellites, centred on $26^{\circ}44'N$ $55^{\circ}54'E$. The signal here is small, with one fringe (~ 3 cm) in both descending-track interferograms and half a fringe (~ 1.5 cm) in the ascending-track interferogram. However, because it lies in the same place and is of similar shape in all three interferograms, we are confident that it represents surface displacements, not atmospheric noise. The lack of a sharp division between displacements towards the satellite and those away from it indicates that whatever slip is occurring at depth does not reach the surface. The fringes are, however, most closely packed along an \sim ESE trend between $26^{\circ}47'N$ $55^{\circ}52'E$ and $26^{\circ}46'N$ $55^{\circ}55'E$, suggesting that this is where the fault projects to the surface.

Together, these observations are consistent with slip on a buried, \sim N-dipping reverse fault. We illustrate this point by calculating displacements for a simple model fault (strike 270° , dip 45° , rake 90° , slip 1 m, length 8 km, top depth 4 km and bottom depth 8 km) in

an elastic half-space (Okada 1985; Funning *et al.* 2005). These are shown (unwrapped) in Fig. 6(a). In each of the x , y and z components, the majority of motion occurs north of the fault. Displacements are antisymmetric about a line perpendicular to the centre of the fault in the x component, but symmetric about the same line in y and z components.

Interferograms comprise the sum of x , y and z components of motion, each resolved onto the satellite LOS pointing vector (Fig. 6b). The z component dominates both interferograms, with the same sign in each case, but the signal is larger in the descending-track interferogram, with its steeper look angle. On the other hand, the y component contributes little to either interferogram; displacements in this direction are almost parallel with both ascending and descending satellite tracks. Finally, the x component is of the opposite sign in the ascending-track interferogram (where the horizontal component of the look direction is \sim E) than in the descending one (where it is \sim W). This moves the peak LOS displacements west in the ascending case, and east in the descending one. A north-dipping reverse fault can thus account for both the larger displacements in the descending-track interferograms, and the difference in the location of peak displacements in ascending and descending cases.

We now model the interferometric data to estimate the earthquake source parameters. We begin by reducing the number of data points in each interferogram from ~ 2 million to ~ 1000 using a quadtree decomposition algorithm (e.g. Jónsson *et al.* 2002). Giving the ascending-track displacements equal weighting to those of the two descending-track interferograms combined, we invert the data using a downhill-simplex algorithm with multiple Monte Carlo restarts (Wright *et al.* 1999). We solve for uniform slip on a rectangular fault in an elastic half-space (Okada 1985), with an elastic shear modulus of 3.23×10^{10} Pa and a Poisson ratio of 0.25. The location, length, top and bottom depths, strike, dip, rake and amount of slip are all allowed to vary in the inversion.

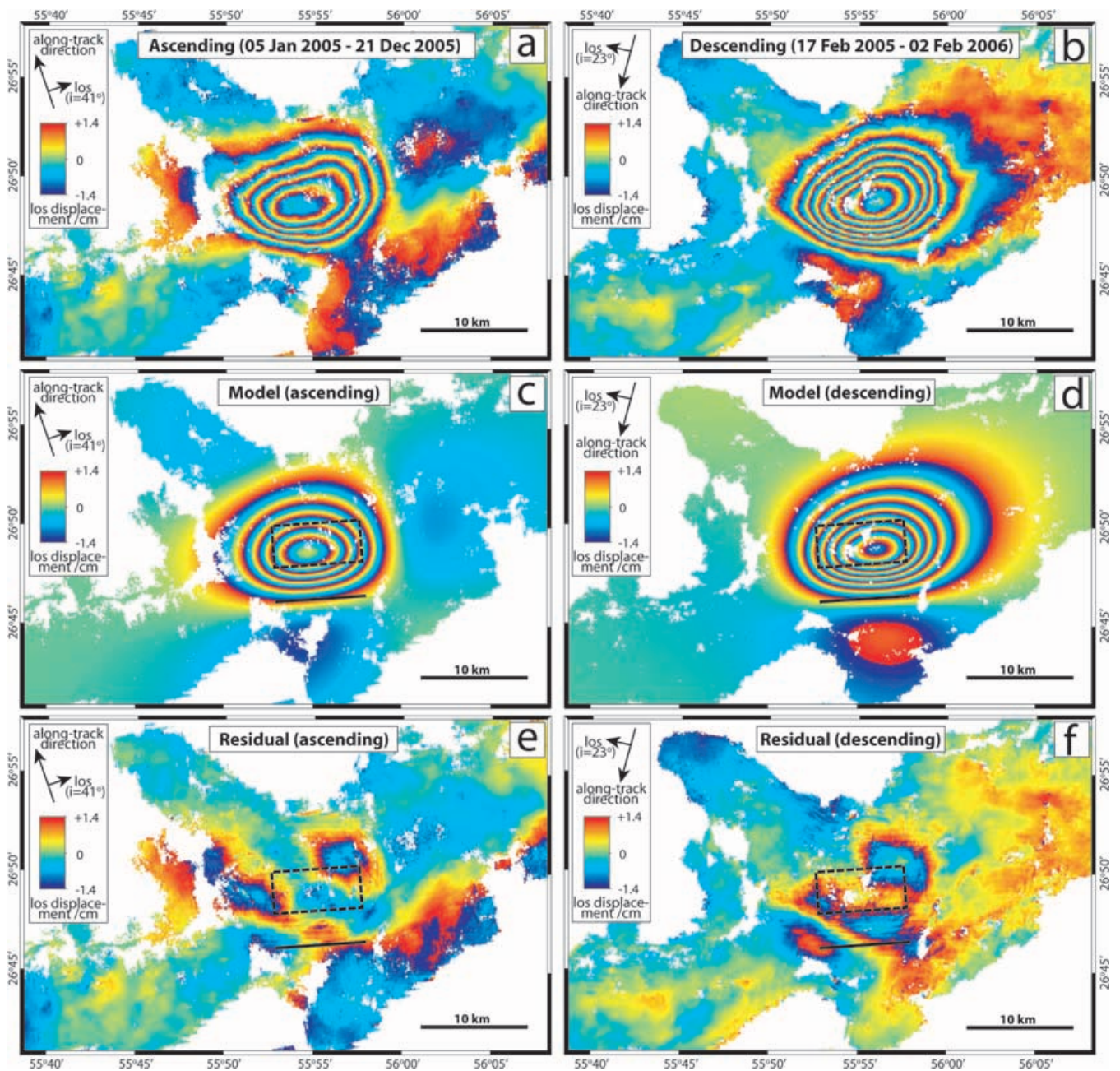


Figure 5. Top: 350-d (a) ascending-track and (b) descending-track interferograms spanning the earthquake. Middle: InSAR-derived model interferograms for (c) ascending and (d) descending cases (parameters in Table 2). Bottom: residuals left by subtracting the model interferogram from the observed one, for (e) ascending and (f) descending cases. All panels are shown wrapped with adjacent fringes differing by 2.8 cm in line-of-sight displacement. The dashed black box show the extents of the buried, north-dipping model fault plane in map view, while the thick black line is its projection at the surface.

The best-fitting model fault parameters are given in Table 2, together with standard deviations calculated by inverting 100 data sets perturbed by realistic noise (Wright *et al.* 2003; Parsons *et al.* 2006). These show ~ 0.9 m of almost pure reverse slip on a fault striking E–W and dipping $\sim 49^\circ$ N. This relatively high angle is typical of reverse-faulting earthquakes in the Zagros, and may be inherited from normal faulting in the stretched Arabian margin, reactivated under the present shortening regime (Jackson 1980, Talebian & Jackson 2003). The model fault plane extends from a maximum depth of ~ 8 up to ~ 4 km beneath the surface. The depth to basement in the SE Zagros has been estimated from aeromagnetic data to be ~ 10 – 17 km (Talebian 2004), although locally there may be

departures from this range. It would appear likely that the fault ruptured the sedimentary sequence, but it is not clear whether or not slip also occurred in the crystalline basement.

Model interferograms are shown in Fig. 5(c) (ascending-track) and Fig. 5(d) (descending-track), with residual interferograms (the difference between observed and model interferograms) in Fig. 5(e) (ascending-track) and Fig. 5(f) (descending-track). There is no more than one fringe present in the residuals, so in general our simple model reproduces the interferometric data well. However, in both ascending and descending cases there are \sim WNW-trending residuals above the western part of our model fault, suggesting a systematic misfit between data and model in this area.

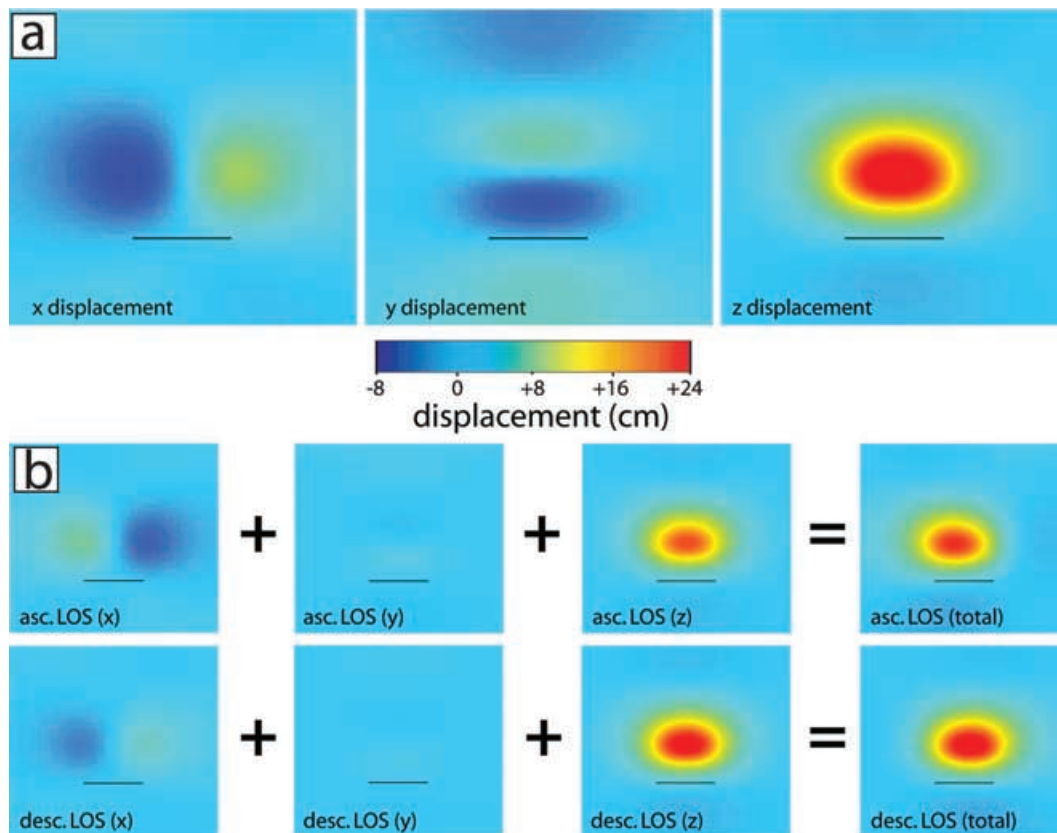


Figure 6. (a) Calculated x , y and z components of motion (unwrapped) for a simple N-dipping, buried reverse fault in an elastic half-space. (b) The same displacements scaled by the satellite line-of-sight (LOS) pointing vectors in ascending (top) and descending (bottom) cases. These sum to produce the observed interferograms. Figure adapted from Funning *et al.* (2005).

Table 2. Fault plane parameters of the 2005 November 27 10:22:19 UTC earthquake from the inversion of interferometric data (with 1σ errors), from P & SH body wave modelling, and as listed in the Harvard CMT and USGS catalogues. Top and Bottom refer to the top and bottom depths of the fault plane, and Centroid is the centroid depth. The first body wave model is the minimum misfit solution; in the second we fixed the centroid depth to 6 km, the equivalent centroid depth of our InSAR model.

Model	Strike	Dip	Rake	Slip (m)	Top (km)	Bottom (km)	Centroid (km)	Length (km)	Moment (Nm)	M_w
InSAR	$267^\circ \pm 2$	$49^\circ \pm 4$	$105^\circ \pm 5$	0.88 ± 0.31	3.9 ± 0.4	8.1 ± 0.4	—	8.4 ± 0.4	$1.27 \times 10^{18} \pm 0.07$	6.0
Body wave	259°	50°	95°	—	—	—	9	—	0.71×10^{18}	5.9
Body wave	250°	50°	91°	—	—	—	6^a	—	0.99×10^{18}	5.9
CMT	257°	39°	83°	—	—	—	12	—	1.03×10^{18}	5.9
USGS	249°	45°	91°	—	—	—	10	—	0.73×10^{18}	5.9

^aDepth fixed during inversion.

These residuals may result from an ambiguity in the strike of the fault. This must account for both the overall E–W elongation of the elliptical pattern of displacements towards the satellite, and the ESE–WNW orientation of the most closely packed fringes (where the fault projects to the surface). Uniform slip on a single, rectangular reverse fault cannot reproduce both of these trends; our model matches the E–W orientation of the ellipse successfully, but leaves residuals trending WNW where the fringes are most closely packed in the interferograms. We find that a two-fault model, with an eastern segment striking \sim W and a western one striking \sim WNW, can reduce the residuals in this area. Allowing distributed slip on the model fault plane would also improve the overall fit to the data. However, for the purposes of this study the simple, uniform-slip, one-fault model reproduces the data sufficiently well.

Finally, we briefly discuss the difference between the 35- and 350-d descending-track interferograms; these contain 6 fringes and 7 fringes of displacements towards the satellite, respectively (Figs 7a

and 5a). This difference is displayed in Fig. 7(b), and may indicate a small amount of ground displacement either before or after the earthquake. To investigate further, we produce two more descending-track interferograms (using the data itemized in the bottom part of Table 1), spanning a \sim 17 month pre-seismic period (Fig. 7c) and a \sim 2 month post-seismic period (Fig. 7d). Both interferograms display small apparent displacements (less than one fringe) towards the satellite, centred close to the peak in the difference interferogram (Fig. 7b) at $26^\circ 49'N 55^\circ 56'E$. However, given the size of these signals it is difficult to demonstrate that these are real ground displacements, not atmospheric noise.

3.3 Teleseismic body wave modelling

The M_w 6.0 and 5.4 earthquakes were widely recorded by stations of the Global Digital Seismic Network (Butler *et al.* 2004). To avoid complications from the Earth's crust and outer core, we use only

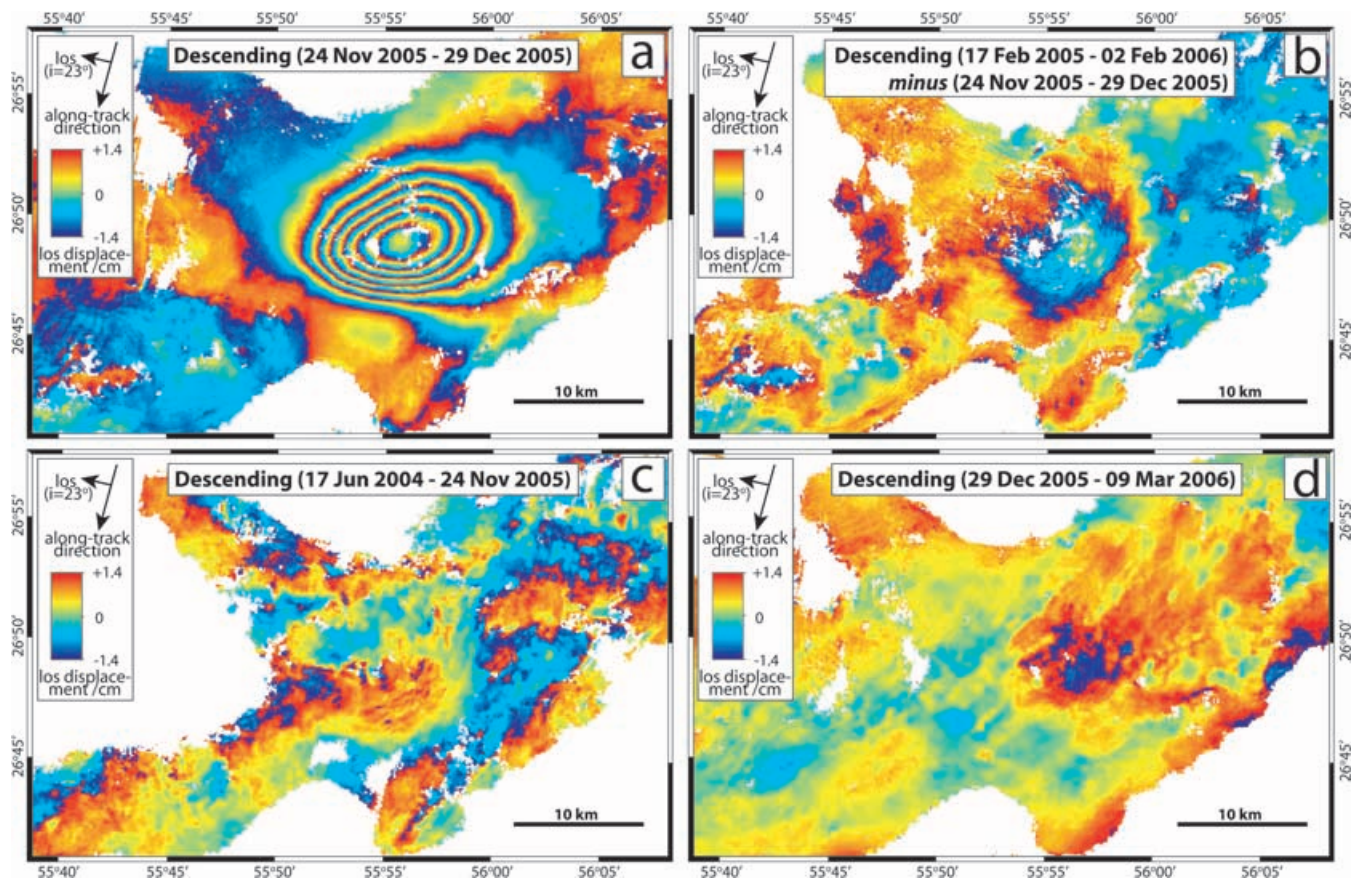


Figure 7. (a) 35-d descending-track interferogram, spanning the earthquake. (b) The difference between the 350- and 35-d descending-track interferograms. (c) Descending-track interferogram spanning ~ 17 months prior to the earthquake. (d) Descending-track interferogram spanning ~ 2 months after the earthquake. All panels are shown wrapped with adjacent fringes differing by 2.8 cm in line-of-sight displacement.

those waveforms recorded in the distance range 30° – 90° . We use the MT5 program (Zwick *et al.* 1994) to invert P and SH waveforms by a weighted least-squares method (McCaffrey & Abers 1988). Our velocity model ($V_p = 6.0 \text{ ms}^{-1}$, $V_s = 3.45 \text{ ms}^{-1}$ and $\rho = 2.78 \times 10^3 \text{ kg m}^{-3}$) is consistent with the elastic parameters used in the interferometric modelling. Following the procedure of Molnar & Lyon-Caen (1989) we obtain the strike, dip, rake, centroid depth, seismic moment and source–time function of the best double-couple solutions.

Our best-fitting body wave model for the larger event is displayed in Fig. 8; from the interferometry, it is clear that the north-dipping nodal plane represents the fault. Source parameters are listed in the second line of Table 2. In addition, we calculate approximate errors of $\sim 10^\circ$ in strike, $\sim 5^\circ$ in dip, $\sim 15^\circ$ in rake and $0.2 \times 10^{18} \text{ N m}$ in moment. These are estimated by fixing individual parameters to a range of values and inverting as previously, before comparing the resulting waveforms with those of the best-fitting solution; they are not formal errors and so are excluded from Table 2. There are negligible differences in strike, dip and rake between our body wave solution and the InSAR model. However, the body wave moment is somewhat lower than the InSAR-derived moment, and the centroid depth (9 km) is deeper than the central point of our InSAR model fault (6 km).

To investigate these discrepancies we run a second body wave inversion with the centroid depth fixed at 6 km (the equivalent centroid depth of our InSAR model). The fit of the P waves in this fixed-depth model is very similar to that in the minimum-misfit so-

lution. The fit of the S waves is worse in the fixed-depth model only for those stations where the fit was poor anyhow; for the stations displaying a simple pulse, the fit is actually better. This improvement is shown in Fig. 9, and leads us to favour a centroid depth of 6 km. Furthermore, the moment of the fixed-depth body wave model is now closer to that of the InSAR model and Harvard CMT mechanism, reflecting a negative trade-off between depth and moment in the seismic modelling; the strike, dip and rake have changed little from earlier minimum-misfit values. The source parameters of our favoured, fixed-depth model are listed on the third line of Table 2.

We do also consider an alternative possibility, that the minimum-misfit body wave centroid depth of 9 km is correct whilst interferometric modelling yields inaccurate top and bottom depths. However, when we produce model interferograms in which the equivalent centroid depth is fixed at 9 km, the fit to the data is significantly degraded. So whereas a centroid depth of 6 km is consistent with both seismic and interferometric data, a depth of 9 km is not.

The best-fitting body wave model for the smaller, 16:30:40 UTC event is shown in Fig. 10. Its source parameters (Table 3) are those of a pure strike-slip fault and lie very close to those of the Harvard CMT solution. Simple forward models of this body wave solution shows that the earthquake is too small to have contributed significantly (more than one fringe) to the interferometric deformation. The interferograms cannot therefore help discriminate between NW- and SW-striking fault planes. Strike-slip faulting is rare in this part of the Zagros, and the aftershock may reflect tearing along the edge of the reverse fault. However, its slip vector (whichever nodal plane

051127A Qeshm
259/50/95/9/7.073E17

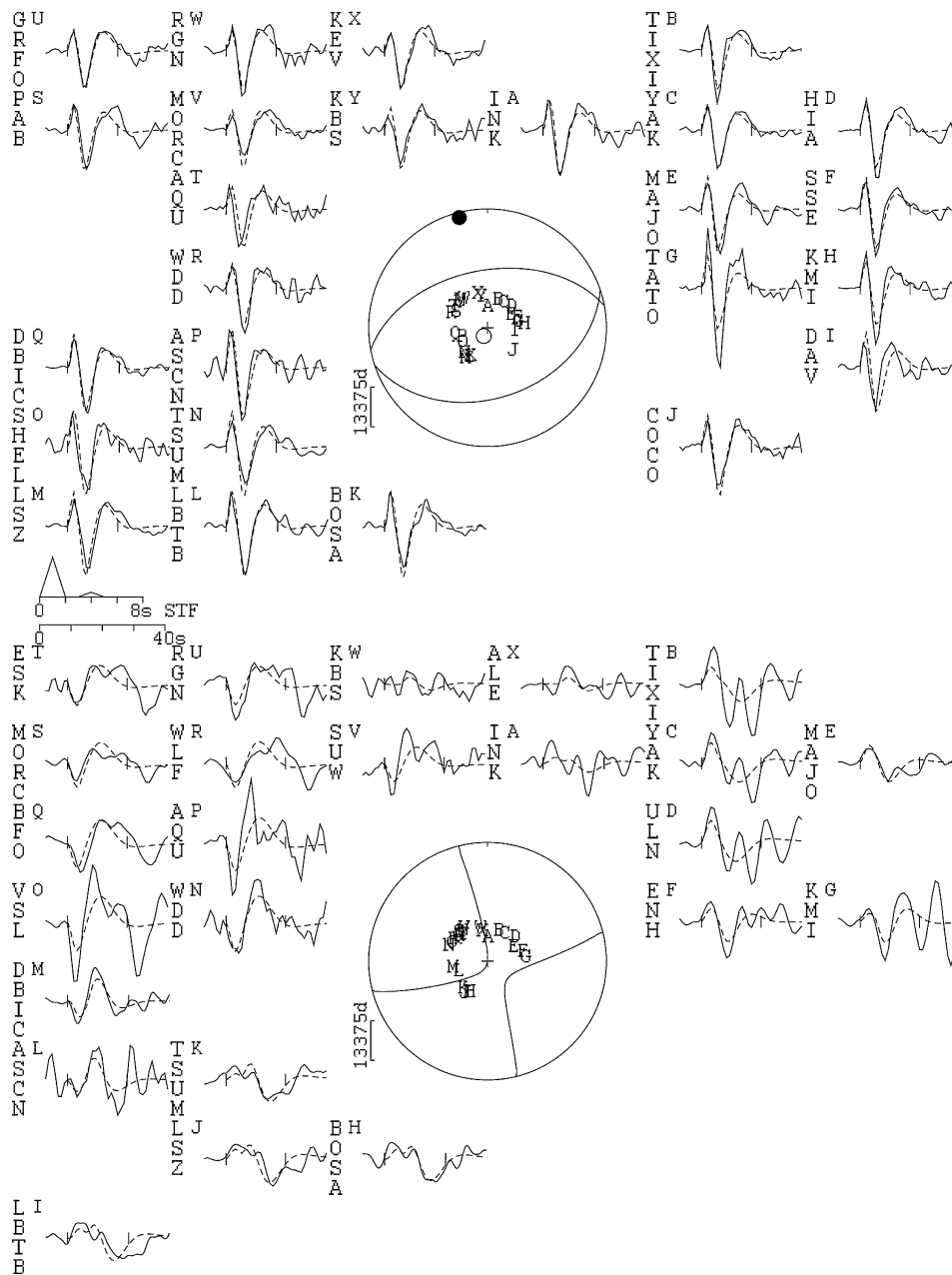


Figure 8. Minimum misfit solution for the 2005 November 27 10:22:19 UTC earthquake, calculated by inverting *P* and *SH* body waves for a point source in a half-space of $V_p = 6.0 \text{ ms}^{-1}$, $V_s = 3.45 \text{ ms}^{-1}$ and $\rho = 2.78 \times 10^3 \text{ kg m}^{-3}$. The focal spheres show *P* (top) and *SH* (bottom) nodal planes in lower hemisphere projections; closed and open circles represent the *P*- and *T*-axes, respectively. Numbers beneath the header line are strike, dip, rake, centroid depth (km) and moment (Nm) of the earthquake. Observed (solid) and synthetic (dashed) waveforms are plotted around the focal spheres; the inversion window is indicated by vertical ticks, station codes are written vertically and station positions denoted by capital letters. The STF is the source–time function, and the scale bar below it (in s) is that of the waveforms.

Table 3. Source parameters of the 2005 November 27 16:30:40 UTC aftershock from *P* and *SH* body wave modelling and as listed in the Harvard CMT catalogue. It is not clear which nodal plane (SW-striking or NW-striking) represents the fault.

Model	Strike1	Dip1	Rake1	Strike2	Dip2	Rake2	Centroid	Moment (Nm)	M_w
Body wave	212°	89°	358°	302°	88°	182°	11 km	1.60×10^{17}	5.4
CMT	218°	87°	358°	308°	88°	183°	12 km	2.13×10^{17}	5.5

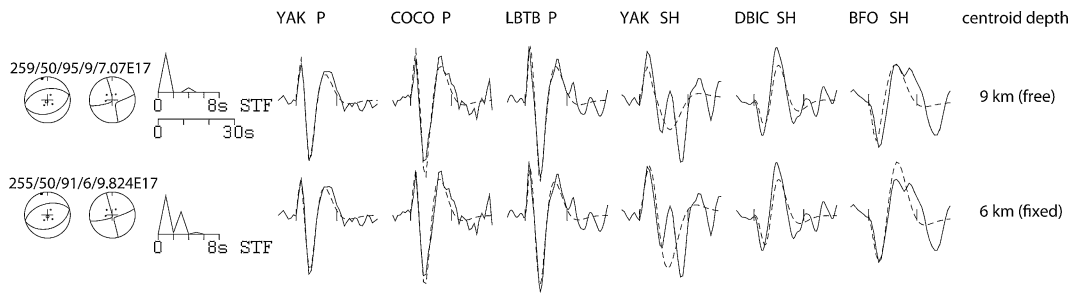


Figure 9. The match between real (solid line) and synthetic (dashed line) waveforms for a selection of three *P* and three *SH* stations, for the minimum misfit solution of the 10:22:19 UTC earthquake (top line) and a model in which the centroid depth was fixed to 6 km (second line). There is a similar match in the *P* waves for the two models; however, where *SH* stations show a simple pulse, such as YAK, DBIC and BFO, the 6 km solution matches the waveforms better than the minimum-misfit one. We therefore prefer the model with a depth of 6 km, which matches the equivalent centroid depth of our InSAR-derived model.

051127B Qeshm aftershock 212/89/358/11/1.603E17

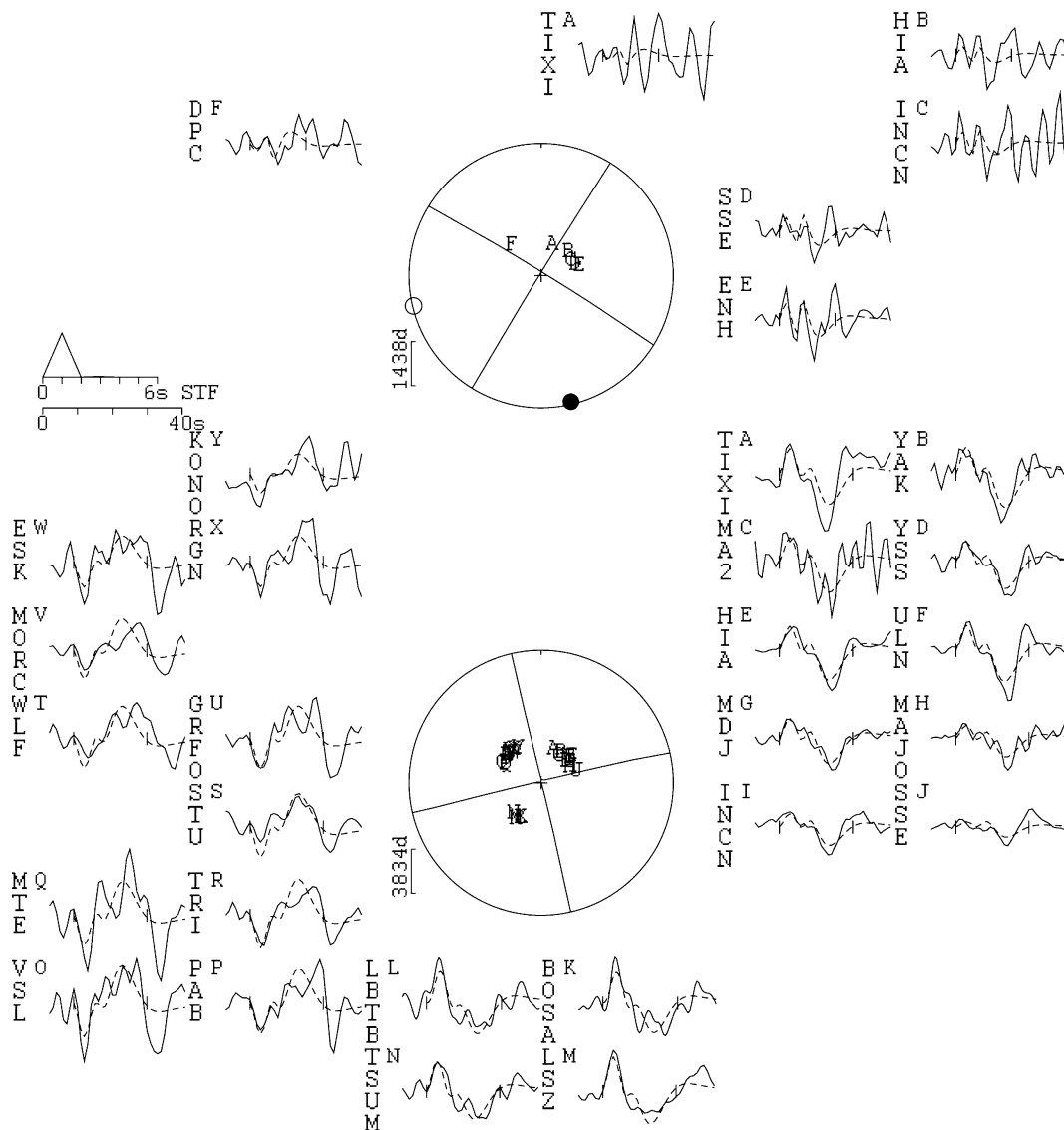


Figure 10. Minimum misfit solution for the 2005 November 27 16:30:40 UTC aftershock. The layout is the same as for Fig. 8.

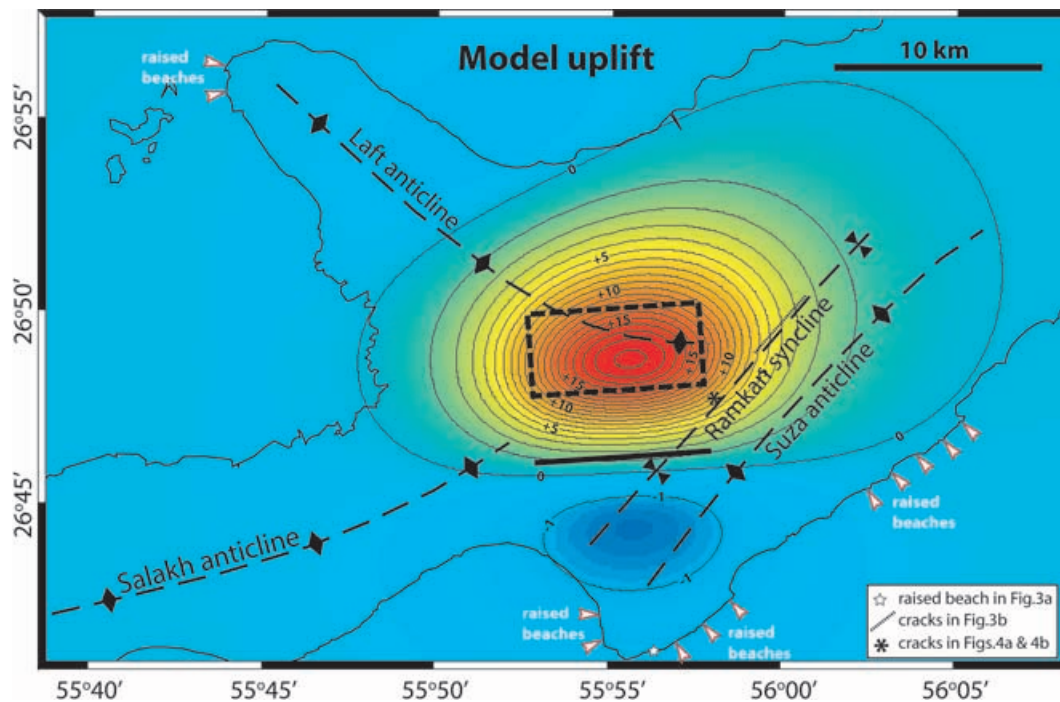


Figure 11. Coseismic uplift computed from our InSAR-derived earthquake model, with contours at 1 cm intervals. The area of positive uplift (up to ~ 20 cm) is centred on the eastern end of the Laft anticline. The dotted black box shows the extents of the buried, north-dipping model fault plane in map view, while the thick black line is its projection at the surface. Raised beaches and surface cracks are given the same symbols as in Fig. 2.

represents the fault) lies oblique to that of the earlier earthquake, so equally this might not be the case.

4 DISCUSSION

A number of simple models of folding exist, with varying degrees of involvement from faulting. In this section, we use the term ‘detachment fold’ to describe those which are completely decoupled from the underlying rock units. Detachment folds have little or no link with faulting, and grow aseptically by buckling in direct response to shortening. The term ‘forced fold’, on the other hand, is used to describe those which grow in direct response to faulting beneath them. Forced folds are typically asymmetric, and can be driven by the upwards propagation of thrust faults at depth or by thrusting of material over bends in the footwall ramp (e.g. Suppe 1983).

In the Zagros Simply Folded Belt many whaleback anticlines have marginally steeper southwestern limbs than northeastern ones. This asymmetry has been used to imply forced folding above NE-dipping thrust or reverse faults (Falcon 1974; McQuarrie 2004). Furthermore, Ramsey *et al.* (2007) present geomorphological evidence that these same anticlines are segmented along length-scales that correspond with the length of faulting expected from the largest earthquakes observed in the Zagros, given simple earthquake scaling relationships; again, this is consistent with forced fold growth. However, others have argued that deformation in the Simply Folded Belt is better explained by detachment folding. Walpersdorf *et al.* (2006) use a discordance between shortening measured with GPS, which is concentrated within ~ 100 km of the Persian Gulf coastline, and seismicity, which extends up to ~ 200 km inland, to suggest decoupling of the sedimentary layers from the basement. Moreover, there are many actively growing folds in the Persian Gulf—hence the existence and continued uplift of islands such as Kish and Sheikh

Shoeyb (Preusser *et al.* 2003)—even though there are very few recent, large earthquakes there.

Of course, it is possible that both models of folding are applicable to the Zagros, and some balanced cross-sections do indeed support a combination of forced folds and décollements (Blanc *et al.* 2003). However taken together, these studies do not conclusively support one type of folding over the other. We now consider whether the deformation observed during the Qeshm Island earthquake can help resolve this problem. In many ways, this earthquake is typical of those in the Zagros Simply Folded Belt: a $M_w \sim 6$ reverse slip event on a steeply dipping ($\sim 50^\circ$) fault plane. Furthermore, slip does not extend to the surface but is buried to ~ 4 km depth.

We use the InSAR model source parameters to produce a map of uplift during the earthquake (Fig. 11). We compare this to the surface structure, displayed on a Landsat image of central Qeshm Island in Fig. 2. The greatest uplift (~ 20 cm), directly above our model fault plane, occurs at the eastern end of the Laft anticline. Here, the fold axis bends E–W, roughly parallel with the model fault. This concurrence hints that the growth of this part of the Laft anticline might be controlled by the buried reverse fault which ruptured in the 2005 earthquake.

However, the pattern of uplift does not contour the Laft anticline but extends eastwards over significant portions of the NE-trending Ramkan syncline and Suza anticline. Together with the compressional cracks in Fig. 3(b), this suggests that these neighbouring folds might also have tightened during the earthquake. The complication here is that only a fraction of the Ramkan and Suza folds uplifted during the earthquake; their long-term growth must be controlled by other factors. Equally, ~ 1 cm coseismic subsidence south of the fault covers the southwestern ends of these same two folds. This subsiding area lies very close to parts of the southern Qeshm coastline that are known to be uplifting over Quaternary timescales (Haghpor & Fontugne 1993).

The faulting involved in the 2005 earthquake might then control the growth of the Laft anticline, but it bears no relation to the shape and long-term growth of neighbouring folds. This argument holds even if we project coseismic slip right up to the surface; if stresses in the top ~4 km were to relax post-seismically by folding along a narrow zone above the fault tip, as is observed above blind thrusts near Los Angeles (Dolan *et al.* 2003), then the pattern of uplift would still fail to reflect long-term fold growth in central Qeshm Island. Of course, there may be other ways in which stresses in the region of folding above the seismogenic faults could relax; certainly there must be more going on than just repeated earthquakes, or the elastic limit would be reached in these uppermost sediments. However, assessing this may require measurements over much longer time periods.

The discordance between vertical motions caused by the earthquake and the pattern of long-term uplift prevents us from convincingly demonstrating a link between faulting and folding on Qeshm Island. Other factors must play a major part in local fold growth, although these could of course include other buried reverse faults. Folding in central Qeshm Island (with orthogonal fold axes) is clearly complicated, and it may take an earthquake in a simpler structural setting to reveal whether there is a one-on-one correlation between faulting and folding in the Zagros.

5 CONCLUSIONS

The M_w 6.0 Qeshm Island earthquake in the Zagros Simply Folded Belt involved reverse slip on a steep (~50°), north-dipping fault plane. Slip was restricted to depths of between ~4 and ~8 km; the earthquake almost certainly ruptured the sedimentary sequence, but whether or not it also affected the uppermost basement is not clear. Coseismic uplift is centred on a prominent anticline, which grew by up to ~20 cm during the earthquake. This implies that the growth of this particular fold is controlled by a reverse fault directly beneath it. However, the pattern of uplift is discordant with the long-term growth of neighbouring folds. On Qeshm Island at least, a simple connection between faulting and folding cannot be made.

ACKNOWLEDGMENTS

This research has been supported by NERC funding of the Centre for the Observation and Modelling of Earthquakes and Tectonics (COMET) (<http://comet.nerc.ac.uk>) and a NERC studentship to EN. We thank M.T. Korehie and the Geological Survey of Iran for organising the fieldwork, and A. Haghypour and the Qeshm Development Organization for their kind hospitality on Qeshm Island. On an earlier trip in January 2005, we were helped by Dr S.H. Tabatabaei, Dr A. Beitollahi and Mr Tahmasebi. Envisat ASAR data were provided by the European Space Agency under project AOE-621, and we are grateful to JPL/Caltech for use of the ROI-PAC software. Finally, we wish to acknowledge John Elliott, Michael Floyd, Ben Fox and Richard Walker for discussions, and two anonymous reviewers for their advice on improving the manuscript.

REFERENCES

- Berberian, M., 1979. Earthquake faulting and bedding thrust associated with the Tabas-e-Golsham (Iran) earthquake of September 16, 1978. *Bull. seism. Soc. Am.*, **69**, 1861–1887.
- Berberian, M., 1995. Master blind thrust faults hidden under the Zagros folds: active basement tectonics and surface morphotectonics, *Tectonophysics*, **241**, 193–224.
- Berberian, M., Jackson, J.A., Qorashi, M., Talebian, M., Khatib, M.M. & Priestley, K., 2000. The 1994 Sefidabeh earthquakes in eastern Iran: blind thrusting and bedding-plane slip on a growing anticline, and active tectonics of the Sistan suture zone, *Geophys. J. Int.*, **142**, 283–299.
- Blanc, E.J.P., Allen, M.B., Inger, S. & Hassani, H., 2003. Structural styles in the Zagros Simply Folded Zone, Iran. *J. Geol. Soc. Lond.*, **160**, 401–412.
- Butler, R. *et al.*, 2004. The Global Seismographic Network surpasses its design goal, *EOS, Trans. Am. geophys. Un.*, **85**, 225–229.
- Dewey, J.W., 1972. Seismicity and tectonics of Western Venezuela, *Bull. seism. Soc. Am.*, **142**, 1711–1751.
- Dolan, J.F., Christofferson, S.A. & Shaw, J.H., 2003. Recognition of paleoearthquakes on the Puente Hills blind thrust fault, California, *Science*, **300**, 115–118.
- Engdahl, E.R., van der Hilst, R. & Buland, R., 1998. Global teleseismic earthquake relocation with improved travel times and procedures for depth determination, *Bull. seism. Soc. Am.*, **3**, 722–743.
- Falcon, N., 1969. Problems of the relationship between surface structure and deep displacements illustrated by the Zagros range, in *Time and Place in Orogeny, Geological Society Special Publications*, **3**, 9–22.
- Falcon, N., 1974. Southern Iran: Zagros Mountains, in *Mesozoic-Cenozoic Orogenic Belts, Geological Society Special Publications*, **4**, 199–211.
- Farr, T. & Kobrick, M., 2000. Shuttle Radar Topographic Mission produces a wealth of data, *EOS, Trans. Am. geophys. Un.*, **81**, 583–585.
- Funning, G.J., 2005. Source parameters of large shallow earthquakes in the Alpine-Himalayan belt from InSAR and waveform modelling, *PhD thesis*, University of Oxford, UK.
- Goldstein, R.M. & Werner, C.L., 1998. Radar interferogram filtering for geophysical applications, *Geophys. Res. Lett.*, **25**, 4035–4038.
- Haghypour, A. & Fontugne, M., 1993. Quaternary uplift of Qeshm Island (Iran), *Comptes Rendus de l'Académie des Sciences, Paris*, **317**(II), 419–424.
- Hessami, K., Koyi, H.A. & Talbot, C.J., 2001. The significance of strike-slip faulting in the basement of the Zagros fold and thrust belt, *J. Petrol. Geol.*, **24**, 5–28.
- Jackson, J.A., 1980. Reactivation of basement faults and crustal shortening in orogenic belts, *Nature*, **283**, 343–346.
- Jónsson, S., Zebker, H., Segall, P. & Amelung, F., 2002. Fault slip distribution of the M_w 7.2 Hector mine earthquake estimated from satellite radar and GPS measurements. *Bull. seism. Soc. Am.*, **92**, 1377–1389.
- King, G.C.P. & Vita-Finzi, C., 1981. Active folding in the Algeria earthquake of 10 October 1980, *Nature*, **292**, 22–26.
- Kent, P.E., 1979. The emergent Hormuz salt plugs of southern Iran, *J. Petrol. Geol.*, **2**, 117–144.
- Kugler, A., 1973. An interpretation of the Southwest Iran aeromagnetic survey. Unpublished 1205, Oil Service Company of Iran.
- Lohman, R.B. & Simons, M., 2005. Locations of selected small earthquakes in the Zagros mountains, *Geochem. Geophys. Geosystems*, **6**(1), doi:10.1029/2004GC000849.
- McCaffrey, R. & Abers, J., 1988. *SYN3: a program for inversion of teleseismic body wave form on microcomputers*, Air Force Geophysical Laboratory Technical Report, AFGL-TR-88-0099, Hanscomb Air Force Base, Massachusetts.
- McQuarrie, N., Stock, J.M., Verdel, C. & Wernicke, B.P., 2003. Cenozoic evolution of Neotethys and implications for the causes of plate motions, *Geophys. Res. Lett.*, **30**, 2036.
- McQuarrie, N., 2004. Crustal scale geometry of the Zagros fold-thrust belt, Iran, *J. Struct. Geol.*, **26**, 519–535.
- Molnar, P. & Lyon-Caen, H., 1989. Fault plane solutions of earthquakes and active tectonics of the Tibetan Plateau and its margins, *Geophys. J. Int.*, **99**, 123–153.
- Morris, P., 1977. Basement structure as suggested by aeromagnetic survey in S.W. Iran. Internal Report, Oil Service Company of Iran.
- Okada, Y., 1985. Surface deformation due to shear and tensile faults in a half-space, *Bull. seism. Soc. Am.*, **75**, 1135–1154.
- Parsons, B. *et al.*, 2006. The 1994 Sefidabeh (eastern Iran) earthquakes revisited: new evidence from satellite radar interferometry and carbonate dating about the growth of an active fold above a blind thrust fault, *Geophys. J. Int.*, **164**, 202–217.

- Preusser, F., Radtke, U., Fontugne, M., Haghypour, A., Hilgers, A., Kasper, H.U., Nazari, H. & Pirazzoli, P.A., 2003. ESR dating of raised coral reefs from Kish Island, Persian Gulf, *Quat. Sci. Rev.*, **22**, 1317–1322.
- Ramsey, L.A., Walker, R.T. & Jackson, J.A., 2007. Fold evolution and drainage development in the Zagros mountains of Fars province, south-east Iran, *Geophys. J. Int.*, in press.
- Reyss, J.L., Pirazzoli, P.A., Haghypour, A., Hatté, C. & Fontugne, M., 1998. Quaternary marine terraces and tectonic uplift rates on the south coast of Iran, in *Coastal Tectonics, Geological Society Special Publications*, **146**, 225–237.
- Robertson, A.H.F., 2000. Mesozoic-Tertiary tectonic-sedimentary evolution of a south Tethyan oceanic basin and its margins in southern Turkey, in *Tectonics and Magmatism in Turkey and the Surrounding Area, Geological Society Special Publications*, **173**, 97–138.
- Rosen, P.A., Hensley, S., Peltzer, G. & Simons, M., 2004. Updated Repeat Orbit Interferometry package released, *EOS, Trans. Am. geophys. Un.*, **85**, 35.
- Sella, G.F., Dixon, T.H. & Mao, A.L., 2002. REVEL: a model for Recent plate velocities from space geodesy, *J. geophys. Res.*, **107** (B4), Art. No. 2081.
- Suppe, J., 1983. Geometry and kinematics of fault-bend folding, *Am. J. Sci.*, **283**, 684–721.
- Talebian, M., 2003. Active faulting in the Zagros mountains of Iran, *PhD thesis*, University of Cambridge.
- Talebian, M. & Jackson, J., 2004. A reappraisal of earthquake focal mechanisms and active shortening in the Zagros mountains of Iran, *Geophys. J. Int.*, **156**, 506–526.
- Talebian, M. *et al.*, 2004. The 2003 Bam (Iran) earthquake: rupture of a blind strike-slip fault, *Geophys. Res. Lett.*, **31**, doi:10.1029/2004GL020058.
- Talebian, M. *et al.*, 2006. The Dahuiyeh (Zarand) earthquake of 2005 February 22 in central Iran: reactivation of an intra-mountain thrust, *Geophys. J. Int.*, **164**, 137–148.
- Tatar, M., Hatzfeld, D., Martinod, J., Walpersdorf, A., Ghafoori-Ashtiany, M. & Chery, J., 2002. The present-day deformation of the central Zagros from GPS measurements, *Geophys. Res. Lett.*, **29**, 1927–1930.
- Vernant, Ph. *et al.*, 2004. Contemporary crustal deformation and plate kinematics in Middle East constrained by GPS measurements in Iran and northern Oman, *Geophys. J. Int.*, **157**, 381–398.
- Walker, R., Jackson, J. & Baker, C., 2003. Surface expression of thrust faulting in eastern Iran: source parameters and surface deformation of the 1978 Tabas and 1968 Ferdows earthquake sequences. *Geophys. J. Int.*, **152**, 749–765.
- Walker, R.T., Andalibi, M.J., Gheitanchi, M.R., Jackson, J.A., Karegar, S. & Priestley, K., 2005. Seismological and field investigations from the 1990 November 6 Furg (Hormozgan) earthquake: a rare case of surface rupture in the Zagros mountains of Iran, *Geophys. J. Int.*, **163**, 567–579.
- Walpersdorf, A. *et al.*, 2006. Difference in the GPS deformation pattern of North and Central Zagros (Iran), *Geophys. J. Int.*, **167**, 1077–1088.
- Wright, T.J., Parsons, B.E., Jackson, J.A., Haynes, M., Fielding, E.J., England, P.C. & Clarke, P.J., 1999. Source parameters of the 1 October 1995 Dinar (Turkey) earthquake from SAR interferometry and seismic body-wave modelling, *Earth planet. Sci. Lett.*, **172**, 23–37.
- Wright, T.J., Lu, Z. & Wicks, C., 2003. Source model for the M_w 6.7, 23 October 2002, Nenana Mountain Earthquake (Alaska) from InSAR, *Geophys. Res. Lett.*, **30**(18), 1974, doi:10.1029/2003GL018014.
- Yielding, G., Jackson, J.A., King, G.C.P., Sinval, H., Vita-Finzi, C. & Wood, R.M., 1981. Relations between surface deformation, fault geometry, seismicity, and rupture characteristics during the El Asnam (Algeria) earthquake of 10 October 1980, *Earth planet. Sci. Lett.*, **56**, 287–304.
- Zwick, P., McCaffrey, R. & Abers, G., 1994. *MT5 Program*, IASPEI Software Library, **4**.